









Hybrid trajectory planning of two permanent magnets for medical robotic applications

Michael Brockdorff¹ , Tomas da Veiga¹ , Joshua Davy¹ ,
Peter Lloyd¹ , James H Chandler¹ , Giovanni Pittiglio^{1,2} ,
Ryan K Mathew^{3,4}  and Pietro Valdastrì¹ 

The International Journal of
Robotics Research
2024, Vol. 0(0) 1–18
© The Author(s) 2024



Article reuse guidelines:

sagepub.com/journals-permissions
DOI: 10.1177/02783649241264844
journals.sagepub.com/home/ijr



Abstract

Independent robotic manipulation of two large permanent magnets, in the form of the dual External Permanent Magnet (dEPM) system has demonstrated the possibility for enhanced magnetic control by allowing for actuation up to eight magnetic degrees of freedom (DOFs) at clinically relevant scales. This precise off-board control has facilitated the use of magnetic agents as medical devices, including catheter-like soft continuum robots (SCRs). The use of multiple robotically actuated permanent magnets poses the risk of collision between the robotic arms, the environment, and the patient. Furthermore, unconstrained transitions between actuation inputs can lead to undesired spikes in magnetic fields potentially resulting in unsafe manipulator deformation. This paper presents a hybrid approach to trajectory planning for the dEPM platform. This is performed by splitting the planning problem in two: first finding a collision-free physical path for the two robotically actuated permanent magnets before combining this with a path in magnetic space, which permits for a smooth change in magnetic fields and gradients. This algorithm was characterized by actuating each of the eight magnetic DOFs sequentially, eliminating any potential collisions and reducing the maximum undesired actuation value by 203.7 mT for fields and by 418.7 mT/m for gradients. The effect of this planned magnetic field actuation on a SCR was then examined through two case studies. First, a tip-driven SCR was moved to set points within a confined area. Actuation using the proposed planner reduced movement outside the restricted area by an average of 41.3%. Lastly, the use of the proposed magnetic planner was shown to be essential in navigating a multi-segment magnetic SCR to the site of an aneurysm within a silicone brain phantom.

Keywords

Magnetic actuation, trajectory generation, path planning, soft continuum robots, permanent magnets

Received 23 January 2024; Revised 24 April 2024; Accepted 30 May 2024

1. Introduction

Magnetic control of robots offers a range of advantages; notably, forces and torques are applied remotely allowing for almost limitless miniaturization. This possibility to reduce robot scale makes magnetic actuation well suited to medical applications. Magnetic actuation has been demonstrated for control of capsules (Kim et al., 2024), surgical tools (Kladko and Vinogradov, 2024), and microrobots (Bozuyuk et al., 2023) amongst others. This offers the potential for navigation (Kim et al., 2019; Jeon et al., 2019) and therefore drug delivery (Wu et al., 2022) or other treatments in previously inaccessible areas (Jeon et al., 2019).

These benefits can be further exploited through magnetically actuated soft continuum robots (SCRs). SCRs have the potential to be transformative in the healthcare field. The physically soft structure of such devices allows for conformity to natural, curvilinear pathways within organs,

and potentially even in extracellular spaces. Minimising disruption of the native anatomy when performing medical procedures has been shown to reduce trauma, pain, and recovery times (Dupont et al., 2021). SCRs have been proven to be effective in applications such as bronchoscopy (Edelmann et al., 2018), cardiovascular interventions (Yang

¹STORM Lab, Institute of Autonomous Systems and Sensing (IRASS), School of Electronic and Electrical Engineering, University of Leeds, Leeds, UK

²Department of Cardiovascular Surgery, Boston Children's Hospital, Harvard Medical School, Boston, MA, USA

³Department of Neurosurgery, Leeds Teaching Hospitals NHS Trust, Leeds, UK

⁴School of Medicine, University of Leeds, Leeds, UK

Corresponding author:

Michael Brockdorff, STORM Lab, University of Leeds, Woodhouse, Leeds LS2 9JT, UK.

Email: elubr@leeds.ac.uk

et al., 2021; Jeon et al., 2019; Ali et al., 2016), and insertion of cochlear implants (Bruns et al., 2020).

For applications requiring highly precise and delicate navigation of convoluted anatomical pathways such as neurosurgery (Figure 1), there is a benefit in moving beyond point control (tip-driven SCRs) towards increased controllable degrees of freedom (DOFs). This characteristic has been demonstrated for pneumatic SCRs among others (Whitesides, 2018) but remains elusive in the realm of magnetic actuation.

Salmanipour and Diller (2018) show how forces and torques can be independently induced on magnetic agents by controlling the magnetic field and gradient. This multi-DOF actuation can be exploited to achieve full shape and pathway control (important for endovascular navigation). Multi-DOF control of magnetic agents has been shown using systems of coils (Boehler et al., 2023; Bruns et al., 2020; Hoang et al., 2021; Hong et al., 2020; Richter et al., 2021; Salmanipour et al., 2021); however, these systems are typically associated with large, static equipment, small workspaces, up-scaling limitations, and high running costs (da Veiga et al., 2020). The use of External Permanent Magnets (EPMs) allows for the generation of magnetic fields and gradients free from these constraints, thus allowing for a larger workspace (Pittiglio et al., 2022) although a single EPM only allows for a maximum of five DOF control (Kim et al., 2019). Multiple points along a magnetic SCR can be controlled by a single EPM when having each segment oppositely magnetized (Lin et al., 2023); however, the overall independently controllable DOFs are still limited to five.

Multi-EPM actuated systems (Carpi and Pappone, 2009; Ryan and Diller, 2017) have demonstrated five and six DOF control, respectively. However, the dual External Permanent Magnet (dEPM) platform, which uses two robotically actuated EPMs as described in Pittiglio et al. (2023), is the only example of an EPM system that has been shown to actuate the minimum eight magnetic DOFs required to independently control the force and torque on a magnetic object within a confined workspace.

Unlike coil-based systems, the use of robotic manipulators to control the pose of EPMs introduces a non-linear relationship between the robot configuration and the resulting magnetic field. This approach often leads to the production of undesired fields and gradients when transitioning between robot poses. This can lead to an inadvertent change in pose of the SCR, potentially altering its navigation, triggering an unintentional release in payload and/or harming the patient (potentially life-threatening in clinical applications such as neurosurgery). Furthermore, the introduction of robotically actuated EPMs into a sensitive environment such as an operating theatre may bring about additional risks if the movement of these devices is not correctly managed.

Trajectory planning involves finding an ideal route from a start point to an end point while avoiding obstacles. Trajectory planning has been widely used in the field of

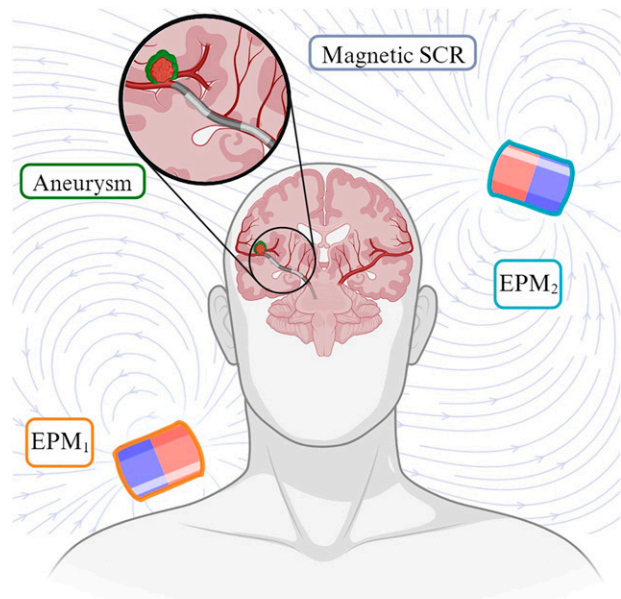


Figure 1. Minimally invasive magnetic robot-assisted surgery allows for access to aneurysms by utilising the brain's native endovascular structure whilst avoiding injury to the brain parenchyma. This illustration demonstrates how a modified SCR can be navigated to the desired location, through which endovascular coiling can be performed (where microcatheter-delivered coils are deployed into the aneurysm, with the aim of blocking blood flow to the aneurysm). This illustration was created using BioRender.com.

robotics, from planning for single multi-DOF robotic manipulators (Ataka et al., 2022; Porges et al., 2021), for multiple robots (Yan et al., 2013), as well as for other medical continuum robots (Hoelscher et al., 2021). Furthermore, neuronavigation is routinely used in neurosurgical clinical practice. Thus, translating trajectory planning using existing brain volumetric imaging, hardware and software is eminently feasible. However, planning to reduce undesired magnetic actuation while avoiding obstacles for the dEPM or similar EPM platforms has yet to be addressed.

This paper introduces a hybrid approach for trajectory planning for the dEPM and similar multi-EPM based platforms. The proposed algorithm takes into account the temporal change in magnetic field space as well as generating a collision-free path in the operational space. The efficacy of this trajectory planner was demonstrated on the dEPM platform where two EPMs are each mounted on a seven-DOF robotic manipulator. Here the objective is to minimize the deviation from the desired magnetic field while preventing collision between the manipulators. This was demonstrated by first analyzing the change in magnetic field and gradient with and without the use of the proposed trajectory planner. The effect of controlled and collision-free magnetic actuation delivered by the trajectory planner was subsequently visualized through two case studies. First, through the control of a SCR with single uniform magnetic segment at its tip. The second case study demonstrates the combined safe operation and predictable magnetic field and

gradient generation in a clinical context by applying the planner to the navigation of a multi-magnet SCR to the site of an aneurysm within a soft brain phantom.

2. Magnetic actuation

An external magnetic field ($\mathbf{B} \in \mathbb{R}^3$) induces a magnetic wrench ($\boldsymbol{\omega} \in \mathbb{R}^6$) on a magnetic agent as follows:

$$\boldsymbol{\omega} = \begin{pmatrix} \mathbf{f} \\ \boldsymbol{\tau} \end{pmatrix} = \begin{pmatrix} (\boldsymbol{\mu} \cdot \nabla) \mathbf{B} \\ \boldsymbol{\mu} \times \mathbf{B} \end{pmatrix} \quad (1)$$

where $\mathbf{f} \in \mathbb{R}^3$ and $\boldsymbol{\tau} \in \mathbb{R}^3$ are the force and torque induced on a magnetic object, respectively, and $\boldsymbol{\mu} \in \mathbb{R}^3$ is the dipole moment of the magnetic agent. For the cylindrical, axially magnetized EPMS used by the dEPM platform the EPMS can be assumed to be a single point in space when the distance is larger than the magnet's radius (Petruska and Abbott, 2013). Using the dipole model and ignoring any higher-order terms, the magnetic field generated by a single EPM in a point in position $\mathbf{r} \in \mathbb{R}^3$ with respect to the origin of EPM is

$$\mathbf{B}(\mathbf{r}, \boldsymbol{\mu}) = \frac{\mu_0 |\boldsymbol{\mu}|}{4\pi |\mathbf{r}|^3} (3\hat{\mathbf{r}}\hat{\mathbf{r}}^T - \mathbb{I})\hat{\boldsymbol{\mu}} \quad (2)$$

Taking the partial spatial derivative of (2), the magnetic gradients can be calculated as

$$\frac{\partial \mathbf{B}(\mathbf{r}, \boldsymbol{\mu})}{\partial \mathbf{r}} = \frac{3\mu_0 |\boldsymbol{\mu}|}{4\pi |\mathbf{r}|^4} ((\mathbb{I} - 5\hat{\mathbf{r}}\hat{\mathbf{r}}^T)(\hat{\mathbf{r}}^T \hat{\boldsymbol{\mu}}) + \hat{\boldsymbol{\mu}} \hat{\mathbf{r}}^T + \hat{\mathbf{r}} \hat{\boldsymbol{\mu}}^T) \quad (3)$$

where \mathbb{I} is the identity matrix, $|\cdot|$ is the Euclidean norm, $\hat{\cdot} = \frac{\cdot}{|\cdot|}$ is the unit vector, and μ_0 is the vacuum magnetic permeability. As there is no significant difference between the vacuum magnetic permeability and that of the human body, we assume that (2) and (3) are representative of the overall environment.

Assuming that the workspace is free from any other magnetic objects and free of currents, Maxwell's equations will apply as

$$\begin{aligned} \nabla \cdot \mathbf{B} &= 0 \\ \nabla \times \mathbf{B} &= 0. \end{aligned}$$

According to these conditions, matrix (3) must be symmetric and have zero trace and therefore can be expanded as

$$\frac{\partial \mathbf{B}(\mathbf{r}, \boldsymbol{\mu})}{\partial \mathbf{r}} = \begin{pmatrix} \frac{\partial B_x}{\partial x} & \frac{\partial B_x}{\partial y} & \frac{\partial B_x}{\partial z} \\ \frac{\partial B_x}{\partial y} & \frac{\partial B_y}{\partial y} & \frac{\partial B_y}{\partial z} \\ \frac{\partial B_x}{\partial z} & \frac{\partial B_y}{\partial z} & -\frac{\partial B_x}{\partial x} - \frac{\partial B_y}{\partial y} \end{pmatrix} \quad (4)$$

As shown by Petruska and Nelson (2015), the gradient matrix (4) thus has five independent components, these being

$$\mathbf{dB}(\mathbf{r}, \boldsymbol{\mu}) = \left(\frac{\partial B_x}{\partial x} \frac{\partial B_x}{\partial y} \frac{\partial B_x}{\partial z} \frac{\partial B_y}{\partial y} \frac{\partial B_y}{\partial z} \right)^T \quad (5)$$

Stacking the field elements with these gradient elements, the eight independently controllable magnetic DOFs can be grouped into the magnetic field vector ($\mathbf{U} \in \mathbb{R}^8$), in the form

$$\mathbf{U}(\mathbf{r}, \boldsymbol{\mu}) = \begin{pmatrix} \mathbf{B}(\mathbf{r}, \boldsymbol{\mu}) \\ \mathbf{dB}(\mathbf{r}, \boldsymbol{\mu}) \end{pmatrix} = \begin{pmatrix} B_x \\ B_y \\ B_z \\ \frac{\partial B_x}{\partial x} \\ \frac{\partial B_x}{\partial y} \\ \frac{\partial B_x}{\partial z} \\ \frac{\partial B_y}{\partial y} \\ \frac{\partial B_y}{\partial z} \end{pmatrix} \quad (6)$$

By substituting (6) into (1) and expressing the $\boldsymbol{\mu}$ and $\boldsymbol{\omega}$ as their components along each axis, the magnet wrench can be written as

$$\boldsymbol{\omega} = \mathbf{S} \mathbf{U} \quad (7)$$

where

$$\mathbf{S} = \begin{pmatrix} 0 & 0 & 0 & \mu_x & \mu_y & \mu_z & 0 & 0 \\ 0 & 0 & 0 & 0 & \mu_x & 0 & \mu_y & \mu_z \\ 0 & 0 & 0 & -\mu_z & 0 & \mu_x & -\mu_z & \mu_y \\ 0 & -\mu_z & \mu_y & 0 & 0 & 0 & 0 & 0 \\ \mu_z & 0 & -\mu_x & 0 & 0 & 0 & 0 & 0 \\ -\mu_y & \mu_x & 0 & 0 & 0 & 0 & 0 & 0 \end{pmatrix}$$

This can be generalized for any number (I) of EPMS by using the superposition principle, such that

$$\begin{aligned} \mathbf{B} &= \sum_{i=1}^I \mathbf{B}_i(\mathbf{r}, \boldsymbol{\mu}) \\ \mathbf{dB} &= \sum_{i=1}^I \mathbf{dB}_i(\mathbf{r}, \boldsymbol{\mu}). \end{aligned} \quad (8)$$

Independent control of each component of \mathbf{U} may be achieved through different EPM configurations (Pittiglio et al., 2023). However, transitions between these configurations tend to cause an undesired coupled actuation between the different components of \mathbf{U} . This is particularly problematic for EPM-based systems where the magnetic field cannot be switched off instantaneously.

3. Motion planning

Before delving into the trajectory planning algorithm proposed, we first define the terms used. Operational space refers to a coordinate system which defines the position and orientation of an object. Magnetic space is defined as the change of magnetic field and gradient with respect to time and position. A path is a set of points in either operational or magnetic space that we intend to follow. A trajectory is defined as a path on which a timing law is specified, typically by means of velocities or accelerations at each point. A trajectory planner algorithm takes a path description along with any constraints (in any domain) and outputs an end-effector trajectory as a time sequence. Using these definitions, we can move on to defining the trajectory planning problem for the dEPM platform.

To avoid undesired cross-activation of magnetic DOFs with EPMS, careful planning of their motions is required. The planner will define a series of poses for each EPM such that the path is collision-free and the magnetic field vector generated throughout the EPMS' trajectory tracks a chosen path in magnetic space. We define the pose of the i^{th} EPM in the operational space as

$$\mathbf{p}_i = \begin{pmatrix} \mathbf{r}_i \\ \phi_i \end{pmatrix} \quad (9)$$

where $\mathbf{r}_i \in \mathbb{R}^3$ represents the positions of the EPM and ϕ_i the orientation described as a quaternion.

The challenge of generating trajectories could be solved by formulating as a differential control problem. Here, the input variables would be defined in joint space (the joint angles of the robots actuating the EPMS) and the Jacobian would be calculated with respect to the applied magnetic field vector in the workspace. However, for this platform, this can lead to solutions which suffer from local minima as well as provoking magnetic instability. The consequence of this being that small variations in the EPMS' position results in large differences in magnetic field.

Another possible approach would be to alter a popular trajectory planning algorithm such as rapidly exploring random trees (Ge et al., 2016; Wei and Ren, 2018), probabilistic road-map planning (Bohlin and Kavraki, 2000; Sánchez and Latombe, 2002; Geraerts and Overmars, 2004) and grid based search methods (Ataka et al., 2022; Sturtevant, 2012) to take into account both a magnetic and positional cost object. However, the exhaustive nature and high time complexity of these algorithms, along with the large number of control variables associated with our system (14 robot joints, 8 magnetic DOFs) combined to make such algorithms inefficient.

Obstacles are easier to describe in operational space than in the corresponding joint space. Additionally, when fidelity to a chosen path in operational space is prioritized, planning directly in task space is suggested (Siciliano et al., 2010). Trajectory planning in operational space ensures the end-effector position is not subject to the non-linear effects introduced by direct kinematics. Thus, we designed our

planning algorithm in operational space and applied standard inverse kinematic solvers for generation of joint space trajectories.

3.1. Planning in operational space

The trajectory planner aims to find a operational space path of EPM poses (Γ_p), where the start pose is the current EPMS' position and orientation and the end pose relates to that required to generate the desired magnetic field vector \mathbf{U}_e . Given the prior knowledge of the start and end poses (through the use of the inverse magnetic solver proposed by Pittiglio et al. (2023) and discussed later in this section), convergence to the desired magnetic field vector is ensured. This allows the planning problem to be split into two parts. The first involves defining a collision-free operational space path for the positions of the EPMS (Γ_r). With EPMS positions defined, the second part subsequently generates a path in magnetic space (Γ_U) that is monotonically increasing or decreasing, as desired (Figure 2). We analytically solve for the orientation of the EPMS such that the magnetic field vector produced along the task space path fits the desired magnetic space path. These two paths can then be combined, under the constraint that both EPMS must complete simultaneously to create the desired trajectory. Splitting the planning problem into two sections helps to preserve the computational tractability of the algorithm by allowing independent optimization of the EPMS' orientation and position. This approach is possible given the high redundancy of our system (2×7 joint angles of the dEPM controlling 8 DOFs in magnetic space), and can be defined mathematically as

$$\Gamma_p = \begin{pmatrix} \Gamma_r \\ \Gamma_U \end{pmatrix} \quad (10)$$

The planning process, along with the transition between spaces can be visualized by the flowchart shown in Figure 2.

3.1.1. EPM position planning. For safe operation of the dEPM platform, two sets of obstacles need to be considered. The first obstacle is a sphere with a radius of 15 cm around the centre of the workspace. This represents the volume in which the magnetically actuated agent will be placed and thus must remain free of both EPMS and robotic manipulators. The second set of obstacles relates to the EPMS themselves. Due to the fact that permanent magnets cannot be 'switched off', it is crucial that each EPM is kept out of the path of, and at a safe distance from, the other EPM. If the EPMS are allowed in close proximity, the magnetic forces and torques may overcome the payload of the robotic manipulators, potentially damaging the robots themselves as well as anyone or anything else present in the workspace. A graphical representation of the dEPM platform and the obstacles considered can be seen in Figure 3.

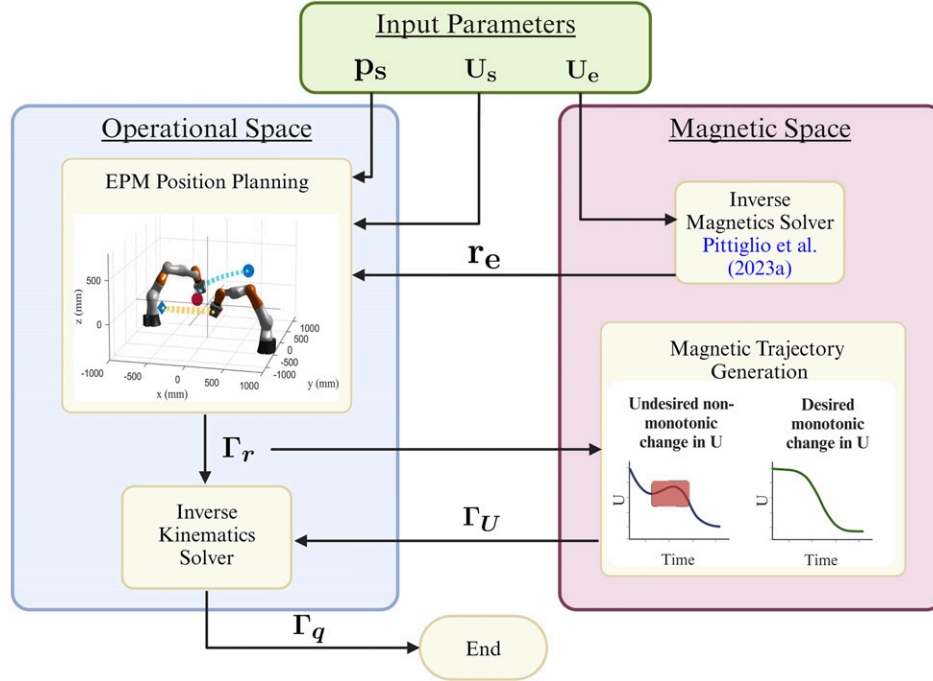


Figure 2. The trajectory planning process visualized through a flowchart. Processes taking part in operational space are grouped in the blue box, while those taking place in magnetic space are grouped in the purple box. The start and end EPM poses (\mathbf{r}_s and \mathbf{r}_e , respectively) along with the desired end magnetic field vector (\mathbf{U}_e) are used to calculate a path of EPM positions (Γ_r) in operational space. The position constraint is then used to optimize the orientation of the EPMS in order to generate the required monotonic magnetic path (Γ_U). Having a monotonic magnetic path ensures that produced magnetic actuation does not fluctuate in opposite direction before converging at \mathbf{U}_e , as it would with a non-monotonic path (shown as a red region). These two paths are then combined to create a series of joint trajectories (Γ_q) for both EPMS.

Considering the symmetry of the dEPM platform and the position of obstacles, we generated an operational space trajectory for the EPMS using spherical coordinates. This allows for easy representation of the obstacle in the middle of the workspace. By applying a spherical constraint to each EPM on opposite sides of the workspace, EPM-to-EPM collision could be easily avoided. The planning task begins by calculating the start position (\mathbf{r}_s) and end position (\mathbf{r}_e) of the EPMS. These positions correlate to the current position of the EPMS and the position that generates the desired magnetic field. As direct analytical inverse solutions are not possible, the position \mathbf{r}_e is found using an optimization approach based on the Levenberg–Marquardt algorithm as described in Pittiglio et al. (2023). This process is referred to as the inverse magnetics solver in Figure 2. The first step is to generate a task space path of positions (Γ_r) which traverses from \mathbf{r}_s to \mathbf{r}_e . This is made up of a series of N points, referred to as waypoints. Therefore Γ_r can be described as

$$\Gamma_r = \mathbf{f}_r(s) \in \mathbb{R}^{3 \times N} \quad (11)$$

where $\mathbf{f}_r(s)$ is a parametric representation of the desired task space path with arc length s , dependent on the number of waypoints chosen.

To create spherical paths between \mathbf{r}_s and \mathbf{r}_e , the function $\mathbf{f}_r(s)$ is one which translates a point into the spherical task space, written as

$$\mathbf{f}_r(s) = \begin{pmatrix} \theta(s) \\ \rho(s) \\ z(s) \end{pmatrix} = \begin{pmatrix} \text{atan2}(y(s), x(s)) \\ \sqrt{x(s)^2 + y(s)^2} \\ z(s) \end{pmatrix} \quad (12)$$

Here, θ , ρ , and z represent the axis of the spherical domain while x , y , and z are the axes of the Cartesian coordinate system, with both these coordinate systems forming part of the operational space. By linearly interpolating between the start and end point in spherical space we ensure that each EPM travels in a circular trajectory around the centre of the workspace, without colliding with the other EPM.

3.1.2. Planning in magnetic space. To allow for a smooth transition in magnetic space, k obstacle-free operational space paths for each EPM are generated with varying values of $\rho(s)$. For every value of s , k different positions are generated. The generation of k different paths gives the opportunity to the motion planning algorithm to choose a waypoint sitting on any one of the generated paths. This allows for a change in EPM position, within a collision-free space, which satisfies the desired change in magnetic actuation. Figure 3 shows the dEPM platform following a trajectory planned to transition between an arbitrary start and end pose with $k = 3$.

Once k paths containing the potential positions of the EPMS have been generated, optimization of the orientation of the EPMS

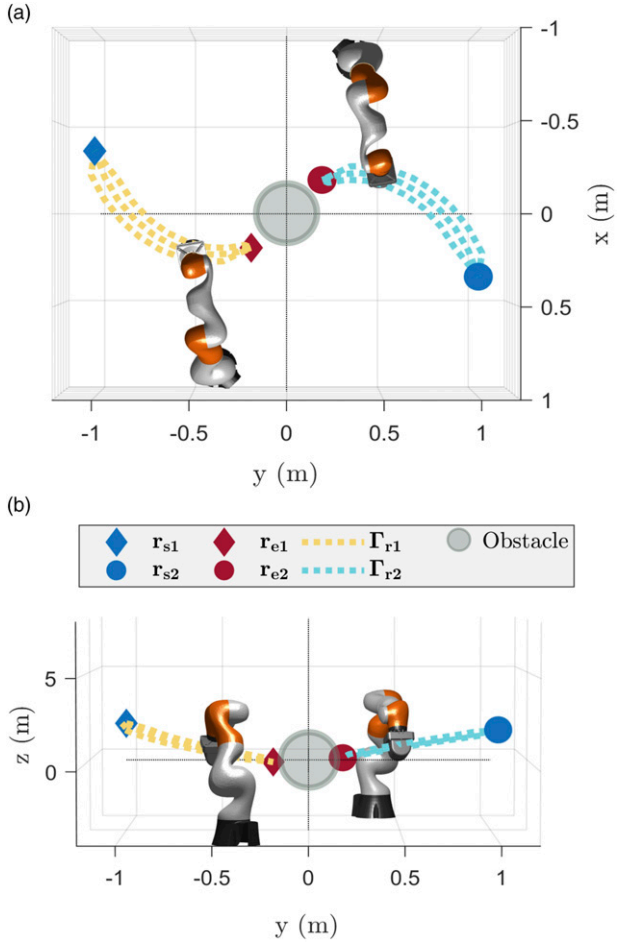


Figure 3. Graphical representation of the dEPM platform, generated paths with $k = 3$ and obstacle in the middle of the workspace. (a) View of platform from above with visualization. (b) View of platform from the Z-Y axis.

can begin. The first step involves creating a desired path in magnetic space (Γ_U). This is the desired change in magnetic actuation between the current EPMS configuration (\mathbf{U}_s) and the desired end magnetic actuation (\mathbf{U}_e). Given the profile of the path of the EPMS, we employed a sigmoid function, whose parameters vary depending on the current waypoint number (n), as the parametric representation of the magnetic path. This is described as

$$\Gamma_U(s) = f_U(s) \in \mathbb{R}^{8 \times n} \quad (13)$$

where

$$f_U(s) = \begin{cases} \mathbf{U}_s & : n = 0 \\ \frac{\mathbf{U}_s}{1 + e^{2.1(s - \frac{n}{2})}} & : n \leq \frac{N}{2} \\ \frac{\mathbf{U}_e}{1 + e^{-2.1(s - \frac{n}{2})}} & : n > \frac{N}{2} \\ \mathbf{U}_e & : n = N \end{cases} \quad (14)$$

The numerical values shown in (14) were empirically tuned. These values represent how quickly the magnetic field changes across the magnetic path. This is dependent on the speed at which the EPMS are physically able to move, and therefore is a platform specific parameter. This produces a magnetic path where the *magnitude* of the generated magnetic actuation ($|\mathbf{U}|$) reduces, then increases, both sigmoidally, in converging on the desired value. This coincides with the expected change in $|\mathbf{U}|$ from moving in a spherical path around the centre of the workspace. The choice in using a combination of monotonic functions (as are the sigmoid functions described in (14)) to define Γ_U allows us to minimize any undesired spiking in $|\mathbf{U}|$ as highlighted by the red region in Figure 2.

Having generated the required EPMS positions through Γ_r and the desired magnetic field through Γ_u , optimization of the orientation of each EPM can begin. First, consider how the magnetic moment $\boldsymbol{\mu}$ is related to the orientation of each EPM through

$$\boldsymbol{\mu}_i = \phi_i \cdot |\mathbf{m}_i| \quad (15)$$

where $|\mathbf{m}_i|$ is the Euclidean norm of magnetic moment of the EPMS. Next, by applying the superposition principle shown in (8), the resulting magnetic field from the two EPMS is

$$\mathbf{B} = \mathbf{B}_1(\mathbf{r}_1, \boldsymbol{\mu}_1) + \mathbf{B}_2(\mathbf{r}_2, \boldsymbol{\mu}_2) \quad (16)$$

where the subscript \cdot_1 refers to EPM 1 and \cdot_2 refers to EPM 2. This can be rewritten as

$$\mathbf{B} = \mathbf{L}(\mathbf{r}_1, \mathbf{r}_2) \begin{pmatrix} \boldsymbol{\mu}_1 \\ \boldsymbol{\mu}_2 \end{pmatrix} \quad (17)$$

where for two EPMS $\mathbf{L} \in \mathbb{R}^{3 \times 6}$. From (2) and (16) \mathbf{L} could be expressed as

$$\mathbf{L}(\mathbf{r}_1, \mathbf{r}_2) = \begin{pmatrix} \frac{\mu_0}{4\pi|\mathbf{r}_1|^3} (3\hat{\mathbf{r}}_1\hat{\mathbf{r}}_1^T - \mathbb{I}) \\ \frac{\mu_0}{4\pi|\mathbf{r}_2|^3} (3\hat{\mathbf{r}}_2\hat{\mathbf{r}}_2^T - \mathbb{I}) \end{pmatrix}^T.$$

Similarly, by applying (4) and (8) to the magnetic gradients generated by two EPMS

$$\mathbf{dB} = \mathbf{M}(\mathbf{r}_1, \mathbf{r}_2) \begin{pmatrix} \boldsymbol{\mu}_1 \\ \boldsymbol{\mu}_2 \end{pmatrix} \quad (18)$$

where for two EPMS, $\mathbf{M} \in \mathbb{R}^{5 \times 6}$. Each j th column of \mathbf{M} could be calculated by substituting $\boldsymbol{\mu}_i$ with

$$\begin{aligned} \boldsymbol{\mu}_1 &= \mathbf{e}_j & \boldsymbol{\mu}_2 &= \mathbf{0}^{3 \times 1} & : j \leq 3 \\ \boldsymbol{\mu}_1 &= \mathbf{0}^{3 \times 1} & \boldsymbol{\mu}_2 &= \mathbf{e}_{j-3} & : j > 3 \end{aligned} \quad (19)$$

and solving for \mathbf{dB} using Equations 3, 4 and 8. Here, the vector \mathbf{e}_j is the j th element of the canonical basis of \mathbb{R}^3 . Therefore, at each waypoint position

$$\Gamma_U(s) = \begin{pmatrix} \mathbf{L}(\mathbf{r}_1, \mathbf{r}_2) \\ \mathbf{M}(\mathbf{r}_1, \mathbf{r}_2) \end{pmatrix} \begin{pmatrix} \boldsymbol{\mu}_1 \\ \boldsymbol{\mu}_2 \end{pmatrix} \quad (20)$$

By knowing the position of each EPM at every waypoint as well as $\Gamma_U(s)$, (20) can be solved for the orientation of each EPM

$$\begin{pmatrix} \boldsymbol{\mu}_1 \\ \boldsymbol{\mu}_2 \end{pmatrix} = \begin{pmatrix} \mathbf{L}(\mathbf{r}_1, \mathbf{r}_2) \\ \mathbf{M}(\mathbf{r}_1, \mathbf{r}_2) \end{pmatrix}^\dagger \Gamma_U(s) \quad (21)$$

where \dagger represents the Moore–Penrose pseudoinverse.

Using (21), $\boldsymbol{\mu}_1$ and $\boldsymbol{\mu}_2$ are calculated to achieve the magnetic actuation dictated by Γ_U at every point of Γ_r . For every value of s , k different values of $\boldsymbol{\mu}$ exist. The resulting value of k which minimizes the difference between $\Gamma_U(s)$ and $\mathbf{U}(s, k)$ are added to $\Gamma_p(s)$. This can be described mathematically as

$$\Gamma_p(s) = \arg \min_k (abs(\Gamma_U(s) - \mathbf{U}(s, k))) \quad (22)$$

Here, the function *abs* refers to the absolute value.

3.2. Joint trajectory generation

By combining operational space and magnetic space planning, optimal trajectories for the EPMS avoiding collisions and producing desired magnetic actuation can be generated. Having found the optimal position and orientation for both EPMS, the next step involves finding the corresponding joint positions for two robots in order to follow the chosen path. Desired joint angles are found via standard inverse kinematic solvers and are constrained to find solutions that avoid collisions between the robot and the central workspace (Robotics Toolbox, MATLAB, MathWorks). Due to the use of a 7 DOF arm to control the 5 DOFs of each EPMS, there is inherent redundancy in kinematic solutions, therefore solutions are constrained to be close in joint space to the previous pose. Once joint space solutions are obtained for the desired poses, they are interpolated using Piece-wise Cubic Hermitean Interpolation Polynomials (PCHIP) (Kahaner et al., 1989) to produce smooth trajectories (Γ_q) between target poses. The joint trajectories have the added constraint that both EPMS must take the same amount of time to complete each path.

3.3. dEPM Platform

The dEPM platform uses two seven-DOF robots manipulating two axially magnetized, cylindrical N52 EPMS (101.6 mm diameter and length) and can be seen in Figure 4(a). This platform is capable of safely generating fields of up to 200 mT and magnetic gradients of up to 500 mT/m. Pittiglio et al. (2023) show how the dEPM platform is capable of accurately generating different combinations of magnetic fields and gradients with 81.1% random field and gradient combinations. Due to the safety risk presented by the unplanned manipulation of the EPMS, the robotic manipulators were restricted to only operate at 30% of their maximum operating speed. The dEPM platform is equipped with a four-camera optical tracking system

(OptiTrack, NaturalPoint, Inc., USA) as seen in Figure 4(a). The tracking setup serves a dual purpose; first, it plays a critical role in calibrating the dEPM platform by determining the centre of actuation. This calibration process involves capturing the position of optical markers strategically placed near the desired centre of actuation. Second, the tracking setup enables real-time monitoring of moving objects (such as SCRs) facilitating the analysis of their positional changes in response to magnetic influence. To make this setup more accommodating for the medical field, these procedures could be replaced by alternative sensing methods such as Fiber Bragg Gratings (FBGs) and magnetic localization.

4. Eight DOF actuation

Independent magnetic field and gradient control is a key factor when controlling magnetic agents. This is due to the possibility to induce independent magnetic forces and torques. Therefore, to determine the performance of the proposed planner, the dEPM platform was subjected to the control task of sequentially actuating every component of (6) independently. Eight different values of \mathbf{U} were actuated in succession, with only one component active at any given time. This equates to the EPMS being sent to eight final poses, each pose actuating a single magnetic field or gradient whilst keeping all other components null. This was done in such a way that the final pose of one actuation forms the start pose of the next trajectory. The magnetic fields were actuated to 10 mT while the magnetic gradients were actuated to 100 mT/m. The actuation order defined in (6) is reproduced below for the reader's convenience.

$$\mathbf{U}_{\text{Act}} = \left(B_x B_y B_z \frac{\partial B_x}{\partial x} \frac{\partial B_x}{\partial y} \frac{\partial B_x}{\partial z} \frac{\partial B_y}{\partial y} \frac{\partial B_y}{\partial z} \right)^T \quad (23)$$

4.1. Methods and experimental setup

The magnetic fields and gradients were measured using the magnetic sensor arrangement shown in Figure 4(b). This consists of three 3D Hall effect sensors (MLX90395, Melexis, Belgium. Sensing range ± 50 mT; Sensitivity $2.5 \mu\text{T}/\text{LSB}_{16}$, Footprint $3 \times 3 \times 0.9$ mm). The position of *sensor*₁ is considered to be in the centre of the workspace. The other sensors were placed a distance $\delta \in \mathbb{R}^3$ from *sensor*₁. The configuration chosen for this experiment involved having *sensor*₂ and *sensor*₃ at a distance of $\delta = 50$ mm along the positive x and positive y axis of *sensor*₁, respectively. The sensors are interfaced with a Raspberry Pi 4B through I2C protocol. Each set of magnetic actuation experiments were performed twice, once with the previously discussed sensor arrangement and once with *sensor*₁ displaced by $\delta = 12$ mm along the positive z axis. This was necessary to measure all the gradient components which were calculated as follows

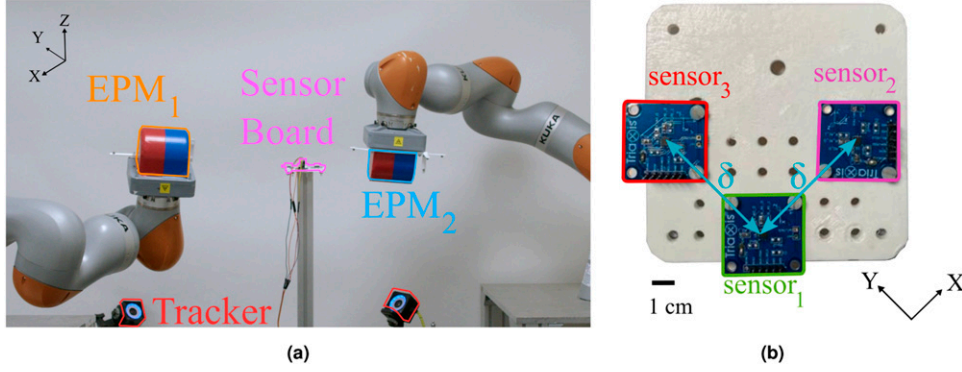


Figure 4. Setup for measuring magnetic fields and gradients. (a) dEPM platform including optical calibration system, with sensor board placed in the middle of the workspace. (b) Sensor board with three 3D Hall effect sensors, used to measure magnetic fields and gradients.

$$\frac{\partial B_m}{\partial n} = \frac{B_{m_1} - B_{m_i}}{\delta_{1_i}} \quad (24)$$

where m and n are the different components of the magnetic gradient, $B_{.i}$ refers to field measurement from the i^{th} sensor and δ_{1_i} is distance between $sensor_1$ and the i^{th} sensor.

4.2. Results

A comparison of the measured magnetic fields and gradients, with and without planning, are presented in Figure 5. For experiments performed without planning, an end pose was specified for each EPM and the default trajectory controller within each robotic manipulator was allowed to formulate the required trajectory. Throughout this paper, this approach is referred to interchangeably by the term *magnetic agnostic planning*. A quantitative analysis of these results can be found in Table 1. The difference in EPMS movement between the two experiments can be seen in Supplemental Video 1. The results between the no planning and the planning experiments were compared by taking an average of the absolute value of the magnetic fields and gradients (where applicable).

Through the use of the trajectory planner, every component of \mathbf{U}_{Act} was actuated sequentially without moving the EPMS to a known position in between. This contrasts to the no planning case, where the EPMS had to be moved to known positions twice in order to avoid a collision with the obstacle in the middle of the workspace. The EPMS' movement while not using the trajectory planner was simulated in the open-source 3D robotics simulator Gazebo and can be seen in Supplemental Video 1.

By further analysing the field and gradients recorded, we can see that the steady state value, that is, the magnetic field or gradient value measured once the EPMS reached their final pose, matched the value set out at the beginning of this experiment for both the no planning and planning scenarios. The error associated with the steady state value (magnetic agnostic planning; 1.5% for fields, 4.4% for gradients, planning; 1.6% for fields, 6.21% for gradients) can be

attributed to the errors related to the optical calibration method used.

The peak off-activation value refers to the maximum magnetic field and gradient measured when no actuation was requested. Table 1 shows that by using the proposed path planner the average peak off-activation can be reduced from 10.1 mT to 2.8 mT for fields and from 382.0 mT/m to 74.0 mT/m for gradients.

The maximum amount by which the magnetic field and gradient overshoot or undershot the desired value during the rise and fall times was also analysed. The rise time is defined as the time from when the change of magnetic field was requested, until steady state activation was recorded. The fall time is defined as the time between when the desired actuation of (23) is set to 0, until a constant value close to 0 (± 0.5 mT or ± 5 mT/m for gradients) was measured. Overshoots are defined as the amount the field or gradient surpassed the desired value, as a percentage of the desired value, while undershoots are the amount by which the magnetic field or gradient was actuated to a negative value, as a percentage of the desired value. In Table 1, undershoots are represented by a '-' sign. The use of the proposed path planner was shown to drop the average overshoot/undershoot value from 73.3% to 13.4% during the rise time, and from 49.2% to 8.8% during the fall time.

The standard deviation (σ) during the off-activation period was also compared. This represents how much the magnetic field and gradient differ from the zero value when no activation is requested. Therefore, a σ of 0 is desired for the optimal case. The magnetic planner reduced the σ from 1.19 mT to 0.45 mT for fields and from 39.49 mT/m to 13.86 mT/m for gradients.

Information on how the activation of a single DOF affects the other DOFs is shown in Figure 6. This figure shows the maximum field or gradient measured during the rise time of each actuation, referred to as cross-activation. This time period was analyzed as it portrays the time when the EPMS are in transition from one pose to another. The measured values are represented as percentages of the desired field or gradient. Two DOFs are shown to be active for each component of \mathbf{U}_{Act} , as the previous DOF will still be active

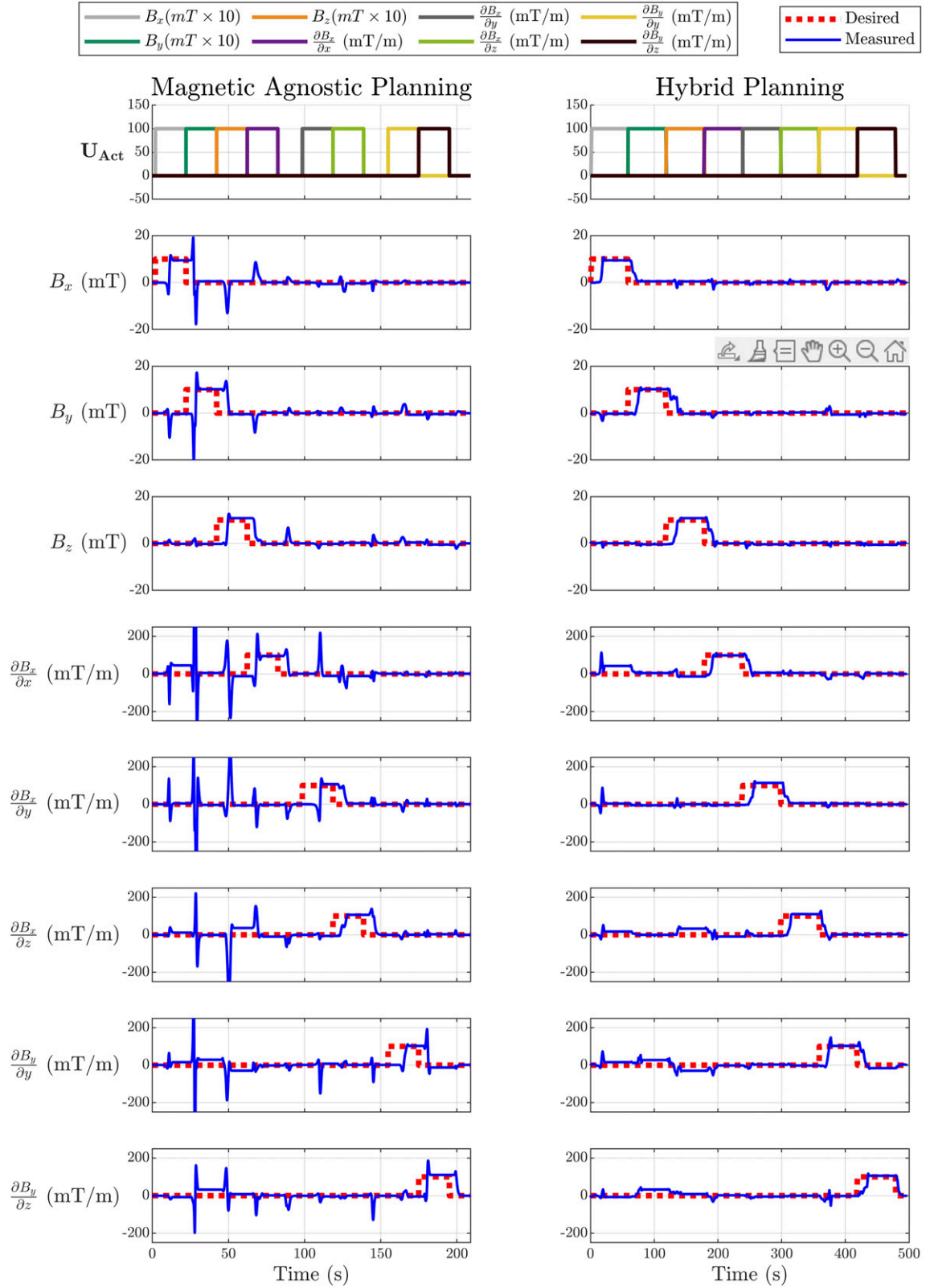


Figure 5. Magnetic fields and gradients using the default magnetic agnostic planning and with the presented hybrid planner. The first row shows the actuation sequence U_{Act} for both experiments. In the magnetic agnostic planning case, U_{Act} had to be altered to have a period with no actuation due to the risk of the EPMS colliding, as seen in [Supplemental Video 1](#). In addition to allowing for the actuation of each component of U_{Act} successively, the use of the trajectory planner also drastically reduced the amount of undesired actuation. The difference in the results obtained is further highlighted in [Table 1](#).

Table 1. Analysis of the magnetic field and gradients measured when successively actuating every component of \mathbf{U}_{Act} . Magnetic fields are displayed in mT while gradients are in mT/m.

		B_x	B_y	B_z	$\partial B_x/\partial x$	$\partial B_x/\partial y$	$\partial B_x/\partial z$	$\partial B_y/\partial y$	$\partial B_y/\partial z$	Average	
										B_i	$\partial B_i/\partial j$
Steady state value	No planning	9.48	10.19	10.79	95.46	106.94	106.43	102.95	110.35	10.15	104.43
	With planning	9.24	10.46	10.77	98.51	113.95	110.12	102.64	105.82	10.16	106.21
Peak off-activation value	No planning	-12.95	-10.47	6.74	409.85	-505.61	-324.85	-479.15	-190.44	10.1	382.0
	With planning	-3.04	-3.31	-2.03	113.11	86.91	43.72	73.06	-53.03	2.8	74.0
Overshoot during rise (%)	No planning	-52.0	-210.1	16.9	123.3	-82.0	0.6	-30.1	71.4		73.3
	With planning	17.0	-6.3	-3.2	-13.8	7.7	-5.5	43.3	10.8		13.4
Overshoot during fall (%)	No planning	-186.5	33.7	-1.2	35.0	3.5	29.9	86.6	17.4		49.2
	With planning	1.57	1.18	0.82	48.31	45.53	38.46	39.45	25.69		8.8
σ during off-activation	No planning	1.57	1.18	0.82	48.31	45.53	38.46	39.45	25.69	1.19	39.49
	With planning	0.52	0.53	0.31	16.70	7.76	13.11	18.06	13.68	0.45	13.86

during the rise time of the next component of \mathbf{U}_{Act} . Figure 6 shows how the proposed planner reduced cross-actuation during EPMs transition.

4.3. Discussion: Hybrid planning approach

In order for the dEPM platform to become a feasible source of actuation in healthcare, effective path planning algorithms will be necessary, in particular, for the actuation of multiple magnetic fields and gradients in succession while having a deterministic change in magnetic field. The importance of this stems from the fact that, particularly in the medical field, the device's movements need to be carried out in a precise manner – any undesired actuation may have potentially harmful results. The algorithm presented in this paper aims to improve robustness and repeatability for magnetically actuated robotic interventions.

This is non-intuitive when using EPMs, due to the highly non-linear relationship between the EPMs' position and the change of magnetic field. The efficiency of the presented algorithm can be expressed in Big O notation as $O(n)$, where n is the number of waypoints. Therefore, the run-time of the hybrid planner is linearly dependent on the number of waypoints. This method is often considered to be the gold standard for performance approximation of an algorithm in terms of the size of the input.

Figure 5 demonstrates how with the presented path planner different magnetic fields and gradients can be actuated successively with minimal undesired actuation. The difference between actuation using the proposed planner compared to classical EPM based actuation techniques is highlighted by Figure 6. It is also important to note that for these experiments, the final EPM pose related to the actuation of each field or gradient at steady state is the same for the planning and no planning case. The path planning

algorithm finds a suitable EPM path which reduces undesired actuation while preventing any collisions.

Our trajectory planning algorithm features two key improvements for managing the operation of magnetically actuated SCR. First, it allows seamless, collision-free, consecutive actuation of fields and gradients, eliminating the need to manually reposition the EPMs to a safe pose between individual actuation steps. Second, despite not completely eliminating undesired actuation, our algorithm minimizes unwanted actuation spikes (shown in Figure 5) which, if unrestricted, could cause notable discrepancies in the movement of a SCR.

The steady state errors highlighted in Table 1 are due to calibration errors in the optical tracking system which reports the position of the magnetic sensors relative to the EPMs. These errors could be reduced through the introduction of a closed loop controller between the magnetic field and gradient generated and the position of the EPMs. The variations in rise and fall phase lags in Figure 5 stem from the requirement for the EPMs to cover differing distances during the actuation of each magnetic field and gradient. Ensuring greater uniformity in the rise and fall times represents a significant focus for the continued development of this algorithm. The use of the trajectory planner significantly reduced the peak off-activation levels, as well as the overshoot during the rise and fall times. These errors were not completely eliminated however with remaining errors attributed to the joint generation section of the proposed trajectory planner. Here, the optimal EPM poses could leave the robotic manipulators in singular positions so slight variations were noted from the expected results.

5. Case study 1: Single-segment SCR

A significant proportion of magnetically actuated SCR typically consist of a single magnetic section with uniform

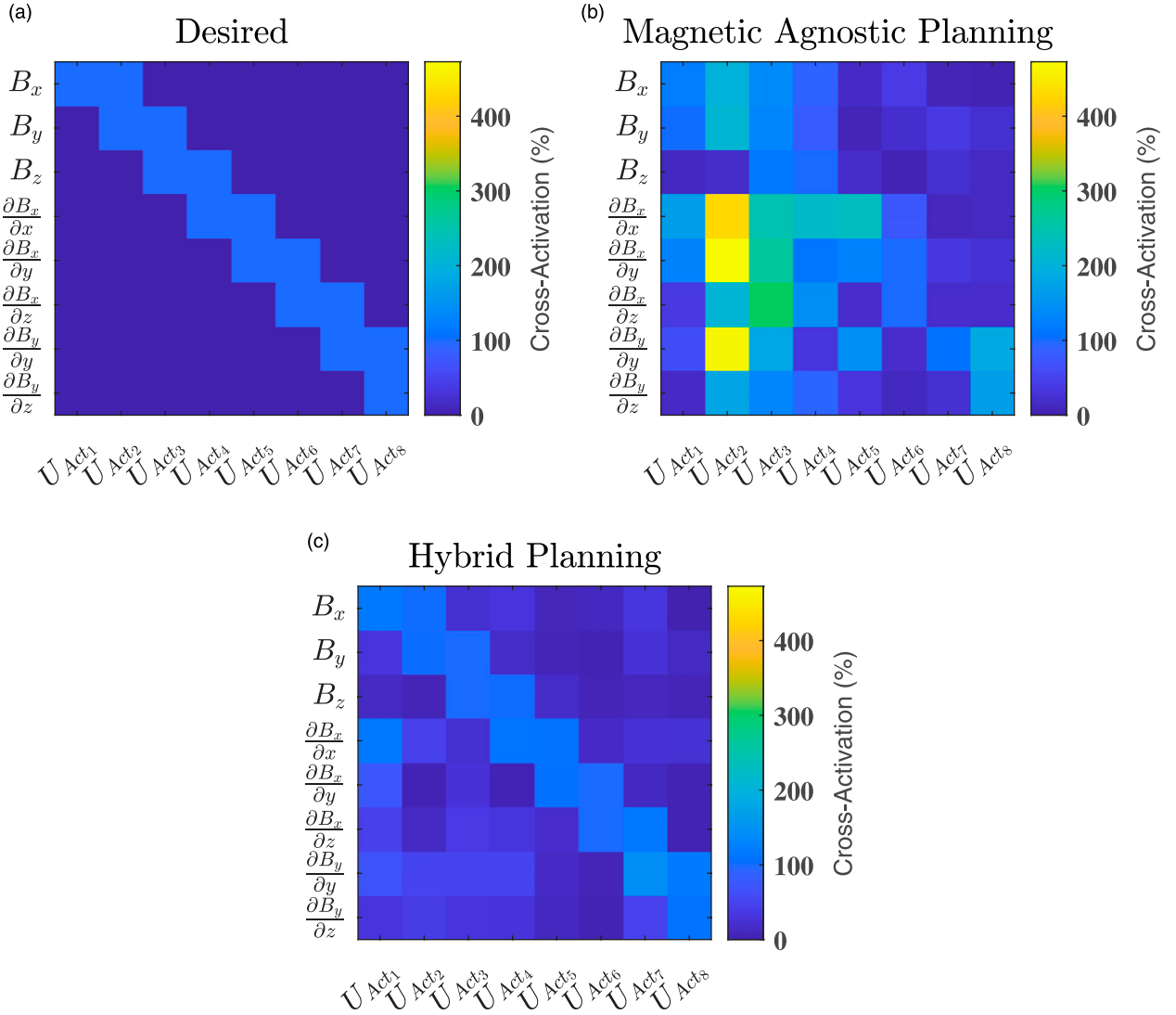


Figure 6. Cross-activation of each U_{Act_i} component during each component’s rise time. These values are represented as a percentage of the desired actuation value. (a) The ideal case is represented by a scenario in which only U_{Act_i} and $U_{Act_{i-1}}$ are active during the transition between the two components. (b) Without the use of the proposed planner (magnetic agnostic planning), a maximum cross-activation of 472.8% was recorded. (c) With the hybrid planner, the maximum cross-activation measured was 143.3%.

magnetization (da Veiga et al., 2020). Here, we demonstrate the efficacy of our dEPM planning approach for actuation of an axially magnetized single-segment SCR. The experiment (Supporting Video 2) shows the precise positioning of the tip of the SCR at four locations, and closely emulates the path taken by a SCR embedded with a laser fibre when ablating a tumour, as previously demonstrated by Kim et al. (2019).

5.1. Single-segment SCR fabrication

For this experiment, we used a cylindrical SCR assembled of two sections; a magnetic tip of length 20 mm and diameter 2 mm, and a silicone overmold (that encapsulates the magnetic tip) of length 70 mm and diameter 2.5 mm. The fabrication process of this SCR is as follows. First, neodymium-iron-boron (NdFeB) micro particles (5 μm diameter, MQFP-B+,

Magnequench GmbH, Germany) were mixed with a silicone-based elastomer (Dragon SkinTM 30, Smooth-On, Inc., USA) in a 1.5:1 mass ratio. The mixture was degassed and mixed in a high vacuum mixer (ARV-310, THINKYMIXER, Japan) at 1400 r/min, 20.0 kPa for 90 s. The degassed material was injection molded into a 3D printed (Tough PLA, Ultimaker S5, USA) 20 mm length, 2 mm diameter cylindrical mold, to make the magnetic tip segment. This was cured in a UV oven for 30 min at 40°C (Form Cure, Formlabs, USA). The cured magnetic agent was then magnetized axially by subjecting it to a uniform saturating magnetic field of 4.644 T (ASCIM-10-30, ASC Scientific, USA). The now magnetized tip was placed into the full 70 mm length, 2.5 mm diameter 3D printed cylindrical overmold. The magnetic tip was held at the distal end of the mold using two, 0.2 mm diameter nitinol (NiTi) wire pieces as shown in Figure 7(a). Silicone was mixed with red silicone die (Silc PigTM, PMS 186C, Smooth-On, Inc., USA),

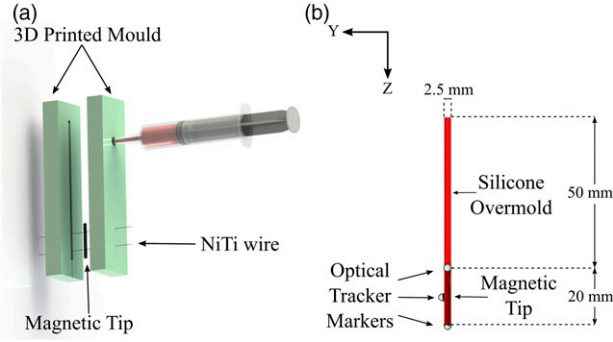


Figure 7. (a) Fabrication of the single-segment SCR. The magnetic tip was held in place with two pieces of NiTi wire whilst a silicone based elastomer (shown in red) was injected into the closed 3D printed mold. (b) Final single-segment SCR after curing. The magnetic tip was facing downwards such that its magnetization is equal to \mathbf{m}_z . Optical tracking markers were used to track the position of the SCR's tip.

with a 1% by weight die-to-silicone ratio. The previous mixing and degassing procedure was repeated before injecting silicone mixture into the 3D printed mold. The injected mold was cured in a UV oven for 30 min at 40°C. The mechanical and elastic properties of the single-segment SCR can be characterized as follows. The magnetic tip has an estimated magnetization vector of 145 kA/m (da Veiga et al., 2021) while the silicone overmold has a linear Elastic Modulus of 593 kPa (Ranzani et al., 2015). We then attached three, 3 mm optical markers (OptiTrack, NaturalPoint, Inc., USA) to the cured SCR using a fast-bonding, high-strength, instant adhesive, to produce the single-segment magnetic SCR shown in Figure 7(b).

5.2. Experimental setup

With the single-segment SCR hanging vertically as shown in Figure 7(b) and in Supporting Video 2, the norm of the magnetic moment can be described as

$$|\mathbf{m}| = (0 \quad 0 \quad 1) = \mathbf{m}_z \quad (25)$$

Knowing the magnetic moment of the SCR, the magnetic fields required to produce the desired deflection direction could be calculated using (7). The demonstration chosen for this experiment required the SCR to reach four spots as shown in Figure 8, following the points in the order 0, 1, 2, 3, 4, 1, with position 0 being the start position. The magnetic field required for the tip of the SCR to reach each point is found in Table 2. Once the desired field combination had been derived, the dEPM platform was tasked with producing the required fields. This was first done by calculating the required poses as described by Pittiglio et al. (2023), then again using the trajectory planning algorithm, described in Section 3 with 10 waypoints between each desired SCR position.

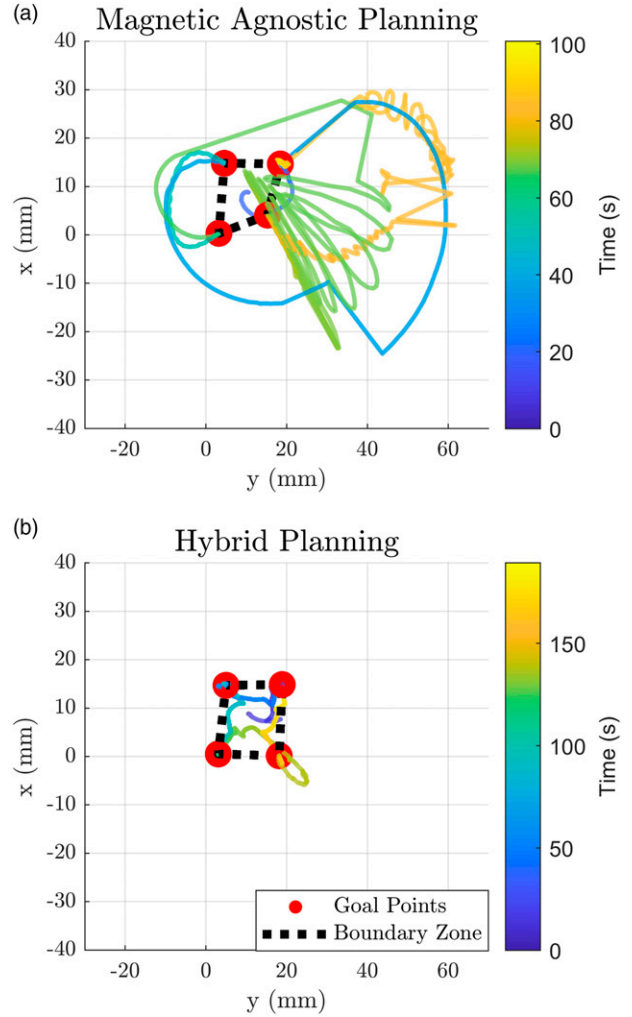


Figure 8. Tip position of a single-segment magnetic SCR in response to the same magnetic fields (a) using the default magnetic agnostic planning (without path planning) and (b) with the hybrid path planner. The tip position measured using the OptiTrack system represented as a coloured line. The colour bar on the right of each figure relates the change in colour to time. Goal points are shown as red dots, and the boundary zone is shown as a black dashed line. Despite using the same desired sequence of magnetic fields in both experiments, the goal points reached in each experiment differ slightly. This is due to undesired torsion in the SCR due to path taken when not using the trajectory planner. A comparison of the different paths taken in the two experiments can be seen in Supplemental Video 2.

5.3. Results

This experiment measures and quantifies the ability of a tip magnetized SCR to move precisely to certain points while staying within a certain area. Figure 8 shows the path taken by the tip of the SCR when tasked with reaching the positions shown in red, while staying in the bounding box (15 mm × 15 mm) shown in a black dashed line, with and without the path planner. The difference in the path taken by the SCR with and without the path planner can also be seen in Supplemental Video 2. The EPMS position relating to the

SCR being at the stable points, shown in red, were the same for both sets of experiments. The difference in stable positions between both experiments resulted from the torsion the SCR experienced when not using the path planner, slightly changing the position of the SCR's tip. A quantification of the error without and with the trajectory planner can be seen in Table 3. The error was measured as the time spent outside of the bounding box. This is presented as a percentage of the total time needed to complete the movement. The total average time where the SCR was outside the predefined box in the no planning case was 74.1%, while under path planning this was reduced to an average of 32.8%.

5.4. Discussion

This experiment highlights the difference between planned magnetic actuation and an arbitrary magnetic transition. The path planner, as observed in Figure 8, helped SCR maintain accurate paths and minimized its tendency to deviate from the estimated trajectory. The data strongly suggests the effectiveness of the path planner in controlling and modulating the SCR's movement, by reducing the time spent outside the predefined area from 74.1% to 32.8%. This is a key feature that can significantly enhance the accuracy and safety of such robots in medical applications such as tumour ablation procedures, where precision and control are paramount. The present algorithm aims to be a first step in the accurate, closed loop control of SCR's motion.

The trajectories of the SCR, as illustrated in Figure 8, demonstrate a stark contrast in the path taken. Without the trajectory planner, the SCR was affected by torsion, resulting in a substantial deviation from the planned route and potentially posing a risk in sensitive medical procedures. However, with the trajectory planner, the SCR's movements were significantly more concise and predictable. Methods to compensate for torsion of SCR when using EPM based actuation without planning have been proposed. These techniques typically require the insertion of a stiffer material through the centre of the SCR (Lloyd et al., 2022) or alter the mechanical design of the SCR (Koszowska et al., 2023) to compensate for torsion in specific directions. This can result in an overall increase in stiffness or diameter of the SCR. In addition, these methods try to eliminate rotation of the SCR around its own axis as a possible DOF. Removing this DOF reduces the possible applications for which SCR could be used, for example, the use of an ultrasound probe where rotation around the long axis may be necessary. The use of the proposed trajectory planning algorithm presents the opportunity to reduce the undesired torsion during magnetic steering of SCR's whilst still maintaining flexibility about this DOF.

6. Case study 2: Navigation of a multi-segment SCR in a soft brain phantom

The capability of independently actuating eight magnetic DOFs, coupled with a non-uniform magnetization profile,

Table 2. Torques and corresponding field required to move the single-segment SCR to each predefined position. Movement directions are given with respect to the dEPM platform's frame, shown in Figure 4(a).

SCR position	Movement direction	Torque	Field (mT)		
			B_x	B_y	B_z
1	+ x-axis	$+\tau_x$	0	-7.5	0
2	- y-axis	$-\tau_y$	-7.5	0	0
3	- x-axis	$-\tau_x$	0	7.5	0
4	+ y-axis	$+\tau_y$	7.5	0	0

Table 3. Time the tip of the SCR spent outside of the bounding box with and without the path planner. Time spent outside is represented as a % of the total time taken to complete the transition.

Section	0-1	1-2	2-3	3-4	4-1
No planning (%)	23.3	83.4	85.2	80.7	98.0
With planning (%)	3.6	46.0	38.7	49.2	26.5

allows for the control of multiple points of a magnetic SCR. An example would be a two-segment SCR with orthogonally magnetized segments. Here, we assume that the two magnetic segments are sufficiently close that the local field experienced by each segment can be assumed to be equal. This two segment control enables lengthwise shape forming of the SCR rather than control of the robot's tip alone. The trajectory planner presented in this paper is applicable to any form of EPMS based actuation. Therefore, we demonstrate the navigational capability of a multi-segment magnetic SCR, actuated using the dEPM platform incorporating the proposed planner. We demonstrate navigation through a complex environment, in this case, a soft phantom of a sample of the vasculature of the brain.

6.1. Soft brain phantom

To demonstrate the enhanced navigational ability of the path planner, a soft brain phantom was manufactured using volumetric Computed Tomography Angiographic (CTA) data from a 47-year-old female with cerebrovascular aneurysms. A segment of the CTA data starting from the middle cerebral artery (MCA) up until the internal carotid artery (ICA) containing terminal ICA aneurysm was selected (Figure 9). The chosen segment of the CTA data was 3D printed (Tough V5 resin, Formlabs II, USA), suspended in a 90 mm by 65 mm acrylic box and then cast in silicone (EcoflexTM Gel, Smooth-On, Inc., USA). This material was chosen due to its Shore hardness of 000-35 closely resembling the bulk behaviour of the brain tissue (Navarro-Lozoya et al., 2019). The silicone was mixed with cure retarder (SLO-JOTM, Smooth-On, Inc., USA) with a ratio of 5% by weight then placed within a vacuum chamber (Renishaw 5/01 vario

vacuum casting machine, Renishaw, United Kingdom) to remove any air bubbles. This was cured at 40°C for 40 min (Genlab Prime, Genlab, United Kingdom). On removal, we had a clear, soft and hollow brain phantom of the cerebral vasculature containing an aneurysm as shown in Figure 9. Optical tracking markers were attached to the base of the acrylic box to aid in the calibration of the dEPM platform.

6.2. Multi-segment SCR fabrication

The SCR used in this demonstration is a cylinder of length 50 mm and diameter 2.5 mm containing two magnetic sections with orthogonal magnetic moments. Each magnetic segment is 20 mm long with a separation of 10 mm between each segment. Fabrication was as described in Section 5.1 until the cured magnetic segments were magnetized, with segment 1 magnetized axially, thus having magnetization $-m_x$ and segment 2 magnetized diametrically, magnetization $-m_z$. The overmolding procedure described in Section 5.1 was then repeated, this time using blue silicone die (Silc Pig™, PMS 2757C, Smooth-On, Inc., USA). The multi-segment SCR described here has the same mechanical and magnetic properties as the single-segment SCR described in Section 5.1.

To enable insertion of the SCR into the soft brain phantom, a 40 mm long, 0.75 mm diameter Nitinol wire was attached to the SCR. The base of the Nitinol wire was attached to a Bowden cable passing through a mechanical introducer (Hybrid Stepper Motor MT-1703HSM168RE, MOTTECH MOTOR Co. LTD, China). This was used to introduce the SCR into the brain phantom at a speed of 1 mm/s. The final multi-segment SCR can be seen in Figure 9(c).

6.3. Experimental setup

Aneurysms along the MCA are typically accessed through a surgical splitting of the sylvian fissure (Ikawa, 2019). To emulate the surgical procedure of removing an aneurysm at the junction between the MCA and the ICA, the multi-segment SCR was inserted from the MCA and navigated to the base of the aneurysm. This path follows a complex three-dimensional trajectory. To address the challenge of determining the necessary magnetic fields and gradients for guiding the multi-segment SCR, we simplified the navigation. This involved decomposing the route into three distinct two-dimensional paths as shown in Figure 9. Using (7), the forces, torques and corresponding magnetic fields and gradients required for each section of the navigation were calculated. The effect of the magnetic actuation on each segment at each section of the navigation is summarized in Table 4.

Table 4 shows how some undesired wrenches (shown in bold) are applied during navigation. In path 1, undesired force in the negative x -direction is applied on segment 2; however, this force is countered by the mechanical introducer. In paths 2 and 3, undesired negative torques around the x -axis are applied to the segment 2. This can result in undesirable twisting of the SCR. A point discussed in Section 5.4.

6.4. Results

The first demonstration of this section involved inserting the multi-segment SCR into the soft brain phantom without any magnetic actuation as shown in Supplemental Video 3. Despite the inherent flexibility and softness of the SCR, when no magnetic fields are applied, the SCR collides with

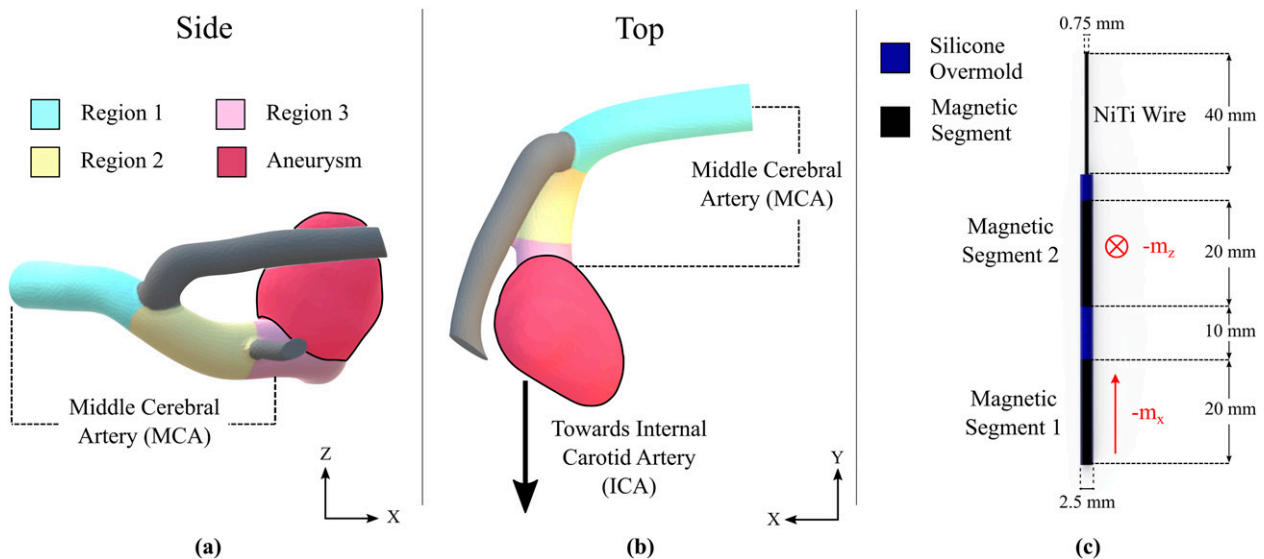


Figure 9. Section of the human brain starting from the middle cerebral artery (MCA) to the internal carotid artery (ICA) containing an aneurysm. Each path of the 3D navigation is shown in a different colour. Seen from the (a) side and (b) top. (c) Multi-segment SCR with orthogonally magnetized segments made for navigation of the soft brain phantom.

Table 4. Magnetic wrench applied to each segment of the multi-segment SCR to navigate the soft brain phantom along with the required field and gradient needed to generate the required wrench. Undesired wrenches are shown in bold. The magnitude of the fields and gradients generated by the dEPM at r_o are shown in the last column, with fields in mT and gradients in mT/m.

Region	Desired		Applied		U	U(r _o)				
	ω_1	ω_2	ω_1	ω_2		B_x	B_y	B_z	$\partial B_x/\partial B_z$	
1	$-\mathbf{f}_z - \tau_y$	0	$-\mathbf{f}_z - \tau_y$	$-\mathbf{f}_x$	$\partial B_x(\mathbf{r})/\partial z + B_z$	$+\partial B_x(\mathbf{r}_o)/\partial B_z$	0	0	0	100
2	$\tau_z - \tau_y$	τ_y	$\tau_z - \tau_y$	$\tau_y - \tau_x$	$-B_x - B_y - B_z$		-12.5	-12.5	-12.5	0
3	τ_y	0	τ_y	$-\tau_x$	$-B_y$		0	-20	0	0

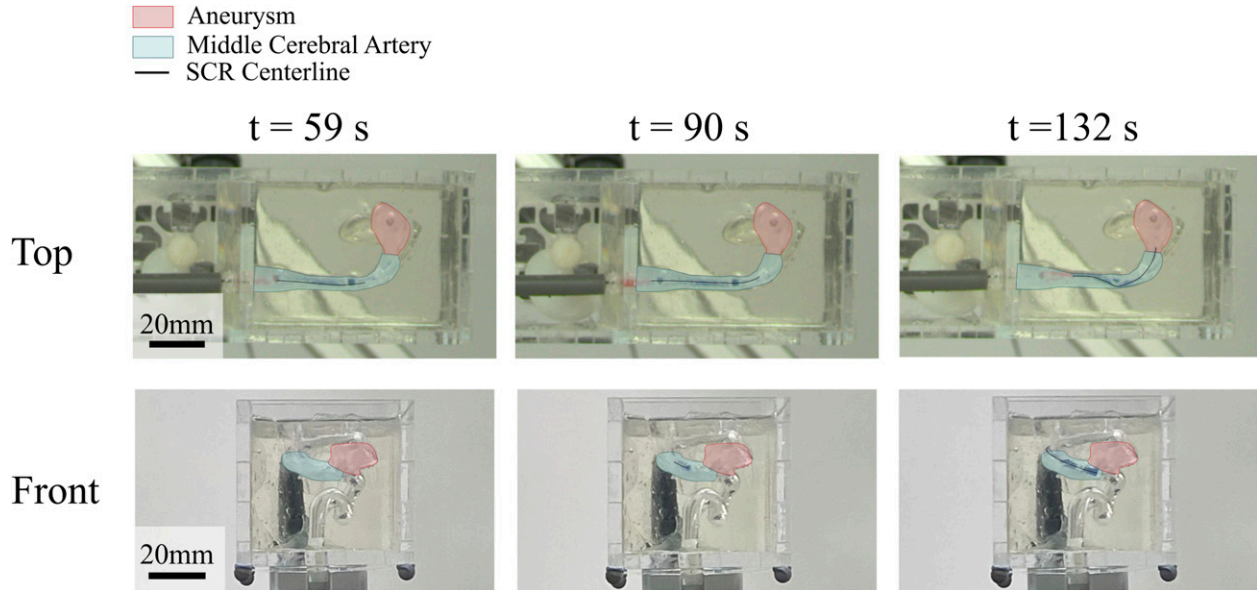


Figure 10. Time series showing the multi-segment magnetic SCR's navigation into the soft brain phantom from three different angles. Using the presented trajectory planner, the SCR (in blue) can be seen to start at the MCA ($t = 59 s$), navigate through the 3D soft brain phantom and arrive at the base of the aneurysm ($t = 132 s$), replicating the path taken by a microcatheter-delivered stent during conventional surgery. Without the use of the trajectory planner, the EPMS collided with the phantom setup. The full 3D navigation with and without the use of the trajectory planner can be seen in [Supplemental Video 3](#).

the walls of the phantom and starts to deform the structures within the phantom as well as buckling on itself.

Using the magnetic fields and gradients in [Table 4](#) along with the trajectory planner (as shown in [Supplemental Video 3](#)) the multi-segment SCR was successfully navigated through the brain phantom to the base of the aneurysm. [Figure 10](#) shows the progression of the SCR through each section of the 3D navigation.

In order to successfully perform the navigation *without* the use of the trajectory planner (as per the convention developed in [Pittiglio et al. \(2022\)](#)), the EPMS were moved to known 'zero' positions between each actuation phase to avoid collisions. Movement to zero positions is not intuitive and often still requires manual planning. This point is highlighted by [Supplemental Video 3](#) where the EPMS inadvertently collided with the phantom, necessitating the activation of the emergency stop button. This shows how the use of the proposed planner will be vital in the safe automation of magnetic SCRs for any practical, medical use.

6.5. Discussion

The rupture of cerebral aneurysms that form along the major arteries within the brain are responsible for approximately 5%–15% of stroke cases ([Brisman et al., 2006](#)). Unprompted rupture of intracranial aneurysms typically leads to subarachnoid hemorrhage. This is a subtype of hemorrhagic stroke with a high mortality rate. Even when non-fatal, the reduction in quality of life associated with subarachnoid hemorrhage remains a cause of physical, psychological, and financial damage in both developing and developed nations ([Chen et al., 2014](#)). One potential solution to re-rupture of aneurysms is endovascular coiling, where microcatheter-delivered coils are deployed into the aneurysm, with the aim of blocking the blood flow to the aneurysm ([Brisman et al., 2006](#)). The coiling mechanism can be stored within the body of the SCR and then be deployed once the navigation process is complete. Alternatively, a magnetic SCR be used as a magnetic guide-wire to navigate standard microcatheter to

a position where such coils could be deployed, as described by Kim et al. (2022).

Navigating delicate and tortuous pathways such as those in the brain, with minimal rates of error, necessitates more comprehensive shape control than mere tip control. Control of multiple points along the SCR's body mitigates potentially painful and damaging contact and deformation along the pathway. This is particularly true when operating in the brain. Here, rupture of any blood vessels can cause hemorrhage which can be potentially fatal. The demonstration presented in this paper illustrates how a trajectory planner that considers both magnetic and Cartesian space-based obstacles can assist in such an environment. The ability to navigate 3D pathways with such precision opens up the possibility to introduce magnetically guided solutions for the treatment of intracranial aneurysms.

7. Conclusions and future work

A trajectory planning algorithm has been developed and implemented on the dEPM platform. The same trajectory planning algorithm could be applied to similar robotically actuated EPM systems with minor adjustments, such as altering the kinematic constraints for the particular manipulator used. This algorithm allows for collision-free operation of two robotically actuated permanent magnets, as well as providing a smooth transition through time variant magnetic fields and gradients.

Experimental deployment of the planner revealed high efficacy, acting on each of the eight magnetic DOFs sequentially to avoid potential collisions, the planner reduced the peak off-activation value by an average of 7.3 mT for fields and by a significant 308 mT/m for gradients relative to the absence of path planning.

To further re-enforce the values of the proposed algorithm in a medical context two case studies were carried out. First, the impact of the planned magnetic fields on the actuation of a SCR was analyzed. Second, a single-segment magnetic SCR was assigned to move towards specific points whilst staying within a prescribed boundary. The proposed planner improved the control on movement of the SCR in the restricted area by an average rate of 41.3%. This is particularly significant where precision is paramount, such as in various surgical procedures. In our final experiment, we demonstrated the medical significance of the proposed path planner by guiding a multi-magnetic segment SCR inside a silicone brain phantom. The results show its effectiveness in the control and navigation of the multi-segment SCR, particularly through such complex environments. This underscores the potential of planned magnetic actuation in steering soft robots without causing collateral damage or deformation of surrounding structures.

This work contributes to the advancement of SCR control, setting a foundation for its automation and broadening its applications in the medical field where precision and safety are crucial. Precise control of a SCR would call for a control system that encompasses both the

SCR's physical properties and the proposed trajectory planning algorithm. The development of this controller extends beyond the boundaries of this study and is earmarked for future work. Future studies could also further enhance this planning algorithm, potentially expanding its application across a broader range of scenarios and systems. The same principles used for the algorithm presented could be scaled for systems with more than two EPMS. Here, the same algorithm may be used with slight adjustments to accommodate a greater number of EPMS and other alterations to the workspace. A further improvement could include adapting the planner to consider mobile obstacles and obstacles not in the centre of the workspace. This would be achieved by dynamically altering the planned route. Once the complexity of the system has been increased, the presented algorithm could be altered to no longer be strictly confined to a spherical shape. Finally, it would be highly desirable to incorporate the planned magnetic actuation into a closed loop shape control algorithm, such as that proposed by Edelmann et al. (2017), modified for multi-segment magnetically actuated SCRs with non-uniform magnetization profiles.

Author's note

Any opinions, findings and conclusions, or recommendations expressed in this article are those of the authors and do not necessarily reflect the views of the EPSRC or the ERC. Website: <https://www.stormlabuk.com/>

Acknowledgements

Special thanks to Mr Samwise Wilson and Dr Dominic Jones for help with experimental arrangements, along with the rest of STORM Lab UK.



Declaration of conflicting interests

The author(s) declared no potential conflicts of interest with respect to the research, authorship, and/or publication of this article.

Funding

The author(s) disclosed receipt of the following financial support for the research, authorship, and/or publication of this article: Research reported in this article was supported by the European Research Council (ERC) under the European Union's Horizon 2020 research and innovation programme (grant agreement No. 818045), by the Engineering and Physical Sciences Research Council (EPSRC) under grant numbers EP/R045291/1, EP/V009818/1 and EP/S009000/1, and by the National Institute for Health and Care Research (NIHR) Leeds Biomedical Research Centre (BRC) (NIHR203331). The views expressed are those of the authors and not necessarily those of the ERC, EPSRC, NIHR or the Department of Health and Social Care.

ORCID iDs

Michael Brockdorff  <https://orcid.org/0000-0001-9022-4670>
 Tomas da Veiga  <https://orcid.org/0000-0002-4286-4590>
 Joshua Davy  <https://orcid.org/0000-0001-9483-111X>

Peter Lloyd  <https://orcid.org/0000-0002-4927-071X>
 James H Chandler  <https://orcid.org/0000-0001-9232-4966>
 Giovanni Pittiglio  <https://orcid.org/0000-0002-0714-5267>
 Ryan K Mathew  <https://orcid.org/0000-0002-2609-9876>
 Pietro Valdastrì  <https://orcid.org/0000-0002-2280-5438>

Supplemental Material

Supplemental material for this article is available online.

References

- Ali A, Plettenburg DH and Breedveld P (2016) Steerable catheters in cardiology: classifying steerability and assessing future challenges. *IEEE Transactions on Biomedical Engineering* 63(4): 679–693. DOI: [10.1109/TBME.2016.2525785](https://doi.org/10.1109/TBME.2016.2525785).
- Ataka A, Lam HK and Althoefer K (2022) Magnetic-field-inspired navigation for robots in complex and unknown environments. *Frontiers in Robotics and AI* 9(February): 1–14. DOI: [10.3389/frobt.2022.834177](https://doi.org/10.3389/frobt.2022.834177).
- Boehler Q, Gervasoni S, Charreyron SL, et al. (2023) On the workspace of electromagnetic navigation systems. *IEEE Transactions on Robotics* 39(1): 791–807. DOI: [10.1109/TRO.2022.3197107](https://doi.org/10.1109/TRO.2022.3197107).
- Bohlin R and Kavraki LE (2000) Path planning using Lazy PRM. *Proceedings - IEEE International Conference on Robotics and Automation* 1(April): 521–528. DOI: [10.1109/ROBOT.2000.844107](https://doi.org/10.1109/ROBOT.2000.844107).
- Bozuyuk U, Ozturk H and Sitti M (2023) The mismatch between experimental and computational fluid dynamics analyses for magnetic surface microrollers. *Scientific Reports* 13(1): 10196. DOI: [10.1038/s41598-023-37332-5](https://doi.org/10.1038/s41598-023-37332-5). <https://www.scopus.com/inward/record.uri?eid=2-s2.0-85162819633&doi=10.1038%2fs41598-023-37332-5&partnerID=40&md5=2c9c68e65f401e7dc1aab0cf7855c065>. Citedby:2 (All Open Access, Gold Open Access, Green Open Access).
- Brisman JL, Song JK and Newell DW (2006) Cerebral aneurysms. *New England Journal of Medicine* 355(9): 928–939. DOI: [10.1056/NEJMra052760](https://doi.org/10.1056/NEJMra052760).
- Bruns TL, Riojas KE, Ropella DS, et al. (2020) Magnetically steered robotic insertion of cochlear-implant electrode arrays: system integration and first-in-cadaver results. *IEEE Robotics and Automation Letters* 5(2): 2240–2247. DOI: [10.1109/LRA.2020.2970978](https://doi.org/10.1109/LRA.2020.2970978).
- Carpi F and Pappone C (2009) Stereotaxis Niobe magnetic navigation system for endocardial catheter ablation and gastrointestinal capsule endoscopy. *Expert Review of Medical Devices* 6(5): 487–498.
- Chen S, Li Q, Wu H, et al. (2014) The harmful effects of subarachnoid hemorrhage on extracerebral organs. *BioMed Research International* 2014: 858496. DOI: [10.1155/2014/858496](https://doi.org/10.1155/2014/858496).
- da Veiga T, Chandler JH, Lloyd P, et al. (2020) Challenges of continuum robots in clinical context: a review. *Progress in Biomedical Engineering* 2(3): 032003. DOI: [10.1088/2516-1091/ab9f41](https://doi.org/10.1088/2516-1091/ab9f41).
- da Veiga T, Chandler JH, Pittiglio G et al (2021) Material characterization for magnetic soft robots. In: 2021 IEEE 4th International Conference on Soft Robotics (RoboSoft), New Haven, CT, USA, 2021, pp. 335–342. DOI: [10.1109/RoboSoft51838.2021.9479189](https://doi.org/10.1109/RoboSoft51838.2021.9479189).
- Dupont PE, Nelson BJ, Goldfarb M, et al. (2021) A decade retrospective of medical robotics research from 2010 to 2020. *Science Robotics* 6(60): eabi8017. DOI: [10.1126/scirobotics.abi8017](https://doi.org/10.1126/scirobotics.abi8017).
- Edelmann J, Petruska AJ and Nelson BJ (2017) Magnetic control of continuum devices. *The International Journal of Robotics Research* 36(1): 68–85. DOI: [10.1177/0278364916683443](https://doi.org/10.1177/0278364916683443).
- Edelmann J, Petruska AJ and Nelson BJ (2018) Estimation-based control of a magnetic endoscope without device localization. *Journal of Medical Robotics Research* 03(1): 1–10. DOI: [10.1142/S2424905X18500022](https://doi.org/10.1142/S2424905X18500022).
- Ge J, Sun F and Liu C (2016) RRT-GD: an efficient rapidly-exploring random tree approach with goal directionality for redundant manipulator path planning. *2016 IEEE International Conference on Robotics and Biomimetics (ROBIO)* 2016(1): 1983–1988. DOI: [10.1109/ROBIO.2016.7866620](https://doi.org/10.1109/ROBIO.2016.7866620).
- Geraerts R and Overmars MH (2004) A comparative study of probabilistic roadmap planners. *Springer Tracts in Advanced Robotics* 7: 43–57. DOI: [10.1007/978-3-540-45058-0_4](https://doi.org/10.1007/978-3-540-45058-0_4).
- Hoang MC, Nguyen KT, Le VH, et al. (2021) Independent electromagnetic field control for practical approach to actively locomotive wireless capsule endoscope. *IEEE Transactions on Systems, Man, and Cybernetics: Systems* 51(5): 3040–3052. DOI: [10.1109/TSMC.2019.2917298](https://doi.org/10.1109/TSMC.2019.2917298).
- Hoelscher J, Fu M, Fried I, et al. (2021) Backward planning for a multi-stage steerable needle lung robot. *IEEE Robotics and Automation Letters* 6(2): 3987–3994. DOI: [10.1109/LRA.2021.3066962](https://doi.org/10.1109/LRA.2021.3066962).
- Hong A, Petruska AJ, Zemmar A, et al. (2020) Magnetic control of a flexible needle in neurosurgery. *IEEE Transactions on Biomedical Engineering* 68(2): 616–627. DOI: [10.1109/TBME.2020.3009693](https://doi.org/10.1109/TBME.2020.3009693).
- Ikawa F (2019) *Surgery of Middle Cerebral Artery (MCA) Aneurysm*. Singapore: Springer Singapore. ISBN 978-981-10-8950-3. DOI: [10.1007/978-981-10-8950-3_15](https://doi.org/10.1007/978-981-10-8950-3_15).
- Jeon S, Hoshiar AK, Kim K, et al. (2019) A magnetically controlled soft microrobot steering a guidewire in a three-dimensional phantom vascular network. *Soft Robotics* 6(1): 54–68. DOI: [10.1089/soro.2018.0019](https://doi.org/10.1089/soro.2018.0019).
- Kahaner D, Moler CB, Nash SG, et al. (1989) *Numerical Methods and Software*. Englewood Cliffs, N.J.: Prentice-Hall. ISBN 0136272584.
- Kim Y, Parada GA, Liu S, et al. (2019) Ferromagnetic soft continuum robots. *Science Robotics* 4(33): 1–16. DOI: [10.1126/SCIROBOTICS.AAX7329](https://doi.org/10.1126/SCIROBOTICS.AAX7329).
- Kim Y, Genevriere E, Harker P, et al. (2022) Telerobotic neurovascular interventions with magnetic manipulation. *Science Robotics* 7(65): eabg9907. DOI: [10.1126/scirobotics.abg9907](https://doi.org/10.1126/scirobotics.abg9907).
- Kim S, Bae S, Lee W, et al. (2024) Magnetic navigation system composed of dual permanent magnets for accurate position and posture control of a capsule endoscope. *IEEE Transactions on Industrial Electronics* 71(1): 739–748. DOI: [10.1109/TIE.2023.3245195](https://doi.org/10.1109/TIE.2023.3245195).

- Kladko DV and Vinogradov VV (2024) Magnetosurgery: principles, design, and applications. *Smart Materials in Medicine* 5(1): 24–35. DOI: [10.1016/j.smain.2023.06.008](https://doi.org/10.1016/j.smain.2023.06.008). URL <https://www.sciencedirect.com/science/article/pii/S259018342300025X>
- Koszowska Z, Brockdorff M, da Veiga T, et al. (2023) Independently actuated soft magnetic manipulators for bimanual operations in confined anatomical cavities. *Advanced Intelligent Systems*: 6, 2300062. DOI: [10.1002/aisy.202300062](https://doi.org/10.1002/aisy.202300062). URL <https://onlinelibrary.wiley.com/doi/abs/10.1002/aisy.202300062>
- Lin D, Chen W, He K, et al. (2023) Position and orientation control of multisection magnetic soft microcatheters. *IEEE/ASME Transactions on Mechatronics* 28(2): 907–918. DOI: [10.1109/TMECH.2022.3213934](https://doi.org/10.1109/TMECH.2022.3213934).
- Lloyd P, Onaizah O, Pittiglio G, et al. (2022) Magnetic soft continuum robots with braided reinforcement. *IEEE Robotics and Automation Letters* 7(4): 9770–9777. DOI: [10.1109/LRA.2022.3191552](https://doi.org/10.1109/LRA.2022.3191552).
- Navarro-Lozoya M, Kennedy MS, Dean D, et al. (2019) Development of phantom material that resembles compression properties of human brain tissue for training models. *Materials* 8: 100438. DOI: [10.1016/j.mtl.2019.100438](https://doi.org/10.1016/j.mtl.2019.100438).
- Petruska AJ and Abbott JJ (2013) Optimal permanent-magnet geometries for dipole field approximation. *IEEE Transactions on Magnetics* 49(2): 811–819. DOI: [10.1109/TMAG.2012.2205014](https://doi.org/10.1109/TMAG.2012.2205014).
- Petruska AJ and Nelson BJ (2015) Minimum bounds on the number of electromagnets required for remote magnetic manipulation. *IEEE Transactions on Robotics* 31(3): 714–722. DOI: [10.1109/TRO.2015.2424051](https://doi.org/10.1109/TRO.2015.2424051).
- Pittiglio G, Lloyd P, da Veiga T, et al. (2022) Patient-specific magnetic catheters for atraumatic autonomous endoscopy. *Soft Robotics* 9: 1120–1133. DOI: [10.1089/soro.2021.0090](https://doi.org/10.1089/soro.2021.0090).
- Pittiglio G, Brockdorff M, da Veiga T, et al. (2023) Collaborative magnetic manipulation via two robotically actuated permanent magnets. *IEEE Transactions on Robotics* 39(2): 1407–1418. DOI: [10.1109/TRO.2022.3209038](https://doi.org/10.1109/TRO.2022.3209038).
- Porges O, Leidner D and Roa MA (2021) Planning fail-safe trajectories for space robotic arms. *Frontiers in Robotics and AI* 8(November): 1–11. DOI: [10.3389/frobt.2021.710021](https://doi.org/10.3389/frobt.2021.710021).
- Ranzani T, Gerboni G, Cianchetti M, et al. (2015) A bioinspired soft manipulator for minimally invasive surgery. *Bioinspiration & Biomimetics* 10(3): 035008. DOI: [10.1088/1748-3190/10/3/035008](https://doi.org/10.1088/1748-3190/10/3/035008).
- Richter M, Venkiteswaran VK and Misra S (2021) Multi-point orientation control of discretely-magnetized continuum manipulators. *IEEE Robotics and Automation Letters* 6(2): 3607–3614. DOI: [10.1109/LRA.2021.3064285](https://doi.org/10.1109/LRA.2021.3064285).
- Ryan P and Diller E (2017) Magnetic actuation for full dexterity microrobotic control using rotating permanent magnets. *IEEE Transactions on Robotics* 33(6): 1398–1409. DOI: [10.1109/TRO.2017.2719687](https://doi.org/10.1109/TRO.2017.2719687).
- Salmanipour S and Diller E (2018) Eight-degrees-of-freedom remote actuation of small magnetic mechanisms. In: Proceedings - IEEE International Conference on Robotics and Automation (ICRA), Brisbane, QLD, Australia, 2018, pp. 3608–3613. DOI: [10.1109/ICRA.2018.8461026](https://doi.org/10.1109/ICRA.2018.8461026).
- Salmanipour S, Youssefi O and Diller ED (2021) Design of multi-degrees-of-freedom microrobots driven by homogeneous quasi-static magnetic fields. *IEEE Transactions on Robotics* 37(1): 246–256. DOI: [10.1109/TRO.2020.3016511](https://doi.org/10.1109/TRO.2020.3016511).
- Sánchez G and Latombe J (2002) Checking in PRM planning: application to multi-robot. *The International Journal of Robotics Research* 21(1): 5–26.
- Siciliano B, Sciavicco L, Villani L, et al. (2010) *Robotics: Modelling, Planning and Control*. Incorporated: Springer Publishing Company. ISBN 1849966346.
- Sturtevant NR (2012) Benchmarks for grid-based pathfinding. *IEEE Transactions on Computational Intelligence and AI in Games* 4(2): 144–148. DOI: [10.1109/TCIAIG.2012.2197681](https://doi.org/10.1109/TCIAIG.2012.2197681).
- Wei K and Ren B (2018) A method on dynamic path planning for robotic manipulator autonomous obstacle avoidance based on an improved RRT algorithm. *Sensors* 18(2). DOI: [10.3390/s18020571](https://doi.org/10.3390/s18020571).
- Whitesides GM (2018) Soft robotics. *Angewandte Chemie International Edition* 57(16): 4258–4273. DOI: [10.1002/anie.201800907](https://doi.org/10.1002/anie.201800907). URL <https://onlinelibrary.wiley.com/doi/abs/10.1002/anie.201800907>
- Wu J, Jiao N, Hu X et al (2022) Chemical/magnetic dual-responsive nanorobots with flower-like structure for drug delivery. In: 2022 IEEE International Conference on Robotics and Biomimetics (ROBIO), Jinghong, China, 2022, pp. 247–252. DOI: [10.1109/ROBIO55434.2022.10011940](https://doi.org/10.1109/ROBIO55434.2022.10011940).
- Yan Z, Jouandeau N and Cherif AA (2013) A survey and analysis of multi-robot coordination. *International Journal of Advanced Robotic Systems* 10: 399. DOI: [10.5772/57313](https://doi.org/10.5772/57313).
- Yang Z, Yang L, Zhang M, et al. (2021) Magnetic control of a steerable guidewire under ultrasound guidance using mobile electromagnets. *IEEE Robotics and Automation Letters* 6(2): 1280–1287. DOI: [10.1109/LRA.2021.3057295](https://doi.org/10.1109/LRA.2021.3057295).